Iraqi Journal of Physics, 2026
https://doi.org/10.30723/ijp.v24i1.1457

Vol. 24, No.1, PP.99-108
P-ISSN: 2070-4003
E-ISSN: 2664-5548

Tuning Plasma Properties for Controlled Ni Nanoparticle Synthesis through Pulsed Laser Ablation

Ahmed M. Alwan[1*] and Ahmed A. Ne'mah[2]
[1]*Department of Physics, College of Science, University of Baghdad, Baghdad, Iraq*
*Corresponding author: Ahmed.Musa2404m@sc.uobaghdad.edu.iq

Abstract

This study methodically investigates the correlation between plasma parameters and the structural properties of Ni nanoparticles synthesized via pulsed laser ablation in liquid (PLAL) at varying laser energies, 600-900 mJ. Optical emission spectroscopy (OES) revealed that increasing laser energy enhanced plasma ionization with electron temperature (Te) rising from 0.262 to 0.334 eV, and electron density (ne) increasing from 5.00×1018 to 5.63×1018 cm^{-3} due to intensified collisional excitation. The plasma conditions directly affected the changes in the size and shape of the crystals, showing that higher temperatures and densities in the plasma lead to bigger and more organised nanoparticles. The X-ray diffraction (XRD) analysis showed that both metallic nickel (Ni) and nickel oxide (NiO) were formed, and the crystal size increased from 17.3 to 25.6 nm. Field emission scanning electron microscopy (FE-SEM) demonstrated that, with increasing plasma energy, nanoparticle size increased from 28.29 to 48.73 nm at 600 mJ and from 46.71 to 66.

Article Info.

Keywords:
PLAL, OES, Plasma Characteristics, Ni NPs, Structural Properties.

Article history:
Received:Mar. 23, 2025
Revised: Jul. 09, 2025
Accepted: Oct.10, 2025
Published:Mar.01,2026

1. Introduction

When comparing alternative nanoparticle manufacturing technologies, plasma offers several benefits, including reduced operating and maintenance costs, quicker processing times, and the absence of waste or hazardous substances [1]. Pulsed laser ablation in liquid (PLAL) has emerged as a versatile technique for synthesizing nanomaterials with controlled structural and morphological properties [2]. Unlike chemical synthesis methods, PLAL does not require stabilizing agents, ensuring high-purity nanoparticles (NPs) [3,4]. This makes it advantageous for applications in diverse fields, including biomedicine, catalysis, and energy storage [5]. Among various transition metal oxides, nickel has attracted considerable attention due to its unique electrical, optical, and magnetic properties [6]. These materials exhibit excellent catalytic activity, high thermal stability, and tunable electronic structures, making them suitable for use in supercapacitors [7], gas sensors [8], and magnetic storage devices [9].

The creation of nanoparticles in PLAL is guided by complex physical and chemical processes that are influenced by laser settings such as pulse energy, wavelength, repetition rate, and pulse duration. The process relies on the interaction of a high-intensity laser pulse with a solid target immersed in a liquid. This interaction generates plasma. The resulting ablation plume contains ionized species, electrons, and excited atoms [12]. Key plasma characteristics, including electron temperature (T_e) and electron density (n_e), play a critical role in determining nanoparticle properties. These parameters are typically determined using the following Boltzmann equation, Eq. (1), which is derived under the assumption of local thermodynamic equilibrium [13]:

$$ln\left[\frac{\lambda_{ji} I_{ji}}{hcA_{ji}g_j}\right] = -\frac{1}{kT}(E_j) + ln\left|\frac{N}{U(T)}\right| \quad (1)$$

where λ_{ji} is the wavelength of the emitted line, N is the number density, U(T)

represents the partition function, $h\upsilon_{ji}$ is the photon energy of the transition, E_j is the excitation energy of the level and k_B is the Boltzmann constant.

The electron density (n_e) is determined using the following Stark broadening equation, Eq. (2)[14]:

$$n_e\,(cm^{-3}) = \left(\frac{\Delta\lambda}{2w_s}\right)N_r \quad \textbf{(2)}$$

where ω_s is the Stark broadening parameter in the standard tables corresponding to the N_i I, 361.94 nm wavelength line for the laser-induced plasma, N_r is the reference electron density, and $\Delta\lambda$ is the line broadening.

The energy distribution within the plasma influences material vaporization, nucleation, and growth, affecting the crystallite size, phase composition, and surface morphology of the synthesized NPs [15]. Optical emission spectroscopy (OES) serves as powerful diagnostic tool for characterizing plasma parameters during laser ablation [16]. By analyzing the emission spectra from excited plasma species, it can obtain crucial information about the energy state of the ablated material [13], enabling correlation between plasma conditions and final of the nanoparticles properties [17]. Understanding these relationships allows optimization of synthesis conditions to achieve desirable characteristics [18]. Laser-Induced Breakdown Spectroscopy (LIBS) is a powerful analytical technique used for the immediate diagnosis of the plasma generated by the laser ablation process. This technique relies on analyzing the spectral emissions from the high-temperature and ionized plasma resulting from focusing a high-energy laser pulse on the sample. LIBS allows for the measurement of fundamental plasma properties such as electron temperature and electron density, which are derived from spectral emissions using Boltzmann plots and Stark broadening, respectively.

The LIBS technology has significantly advanced in recent years, with recent studies contributing to the improvement of plasma parameter measurement accuracy. For example, research using the picosecond laser has demonstrated how to precisely control electron density and temperature by adjusting laser parameters [19]. The developed temporal studies have also contributed to the precise determination of Stark broadening coefficients [20]. Additionally, LIBS technology has been applied in advanced environmental and industrial fields, such as detecting heavy metals in soil and water using calibration-free methodologies [21].

In this research, we use the LIBS technique as a diagnostic tool during the synthesis of nickel nanoparticles to determine the relationship between laser energy and the accompanying plasma properties, and then correlate it with the properties of the resulting nanoparticles. The novelty of this research lies in developing an integrated methodology that demonstrates, for the first time, a direct and simultaneous link between plasma diagnostics OES and the properties of nickel/nickel oxide (Ni/NiO) nanoparticles synthesized by PLAL. ln contrasts previous studies that focused solely on post-synthesis characterization, this work introduces a quantitative analytical system that predicts nanoparticle characteristics (size, crystallinity, phase composition) based on in-situ measurements of plasma parameter (T_e, n_e) during the fabrication process. The key innovation is the precise control of Ni/NiO ratio through laser energy modulation (600-900 mJ), enabled by our advanced real-time monitoring platform. This breakthrough with programmable properties is particularly relevant for catalytic and energy storage applications, where phase composition critically determines performance. While the current methodology is optimized for aqueous matrices, the fundamental framework is readily adaptable to organic solvents, as suggested by our preliminary theoretical analysis. This adaptability will be systematically investigated in future research efforts, addressing the scientific challenge of plasma-liquid in non-aqueous system.

2. Experimental Work

In this investigation, LIBS was used. It is made up of an optical emission spectrometer coupled with a laser system. The experimental setup utilized an Nd:YAG laser (Diamond-288) operating fundamental wavelength of 1064 nm with a repetition rate of 5 Hz, pulse duration of 8 ns and different pulsed energies (600, 700, 800, and 900 mJ) to generate plasma. The laser spot was focused on the target through fused silica lens positioned 10 cm from the sample surface, with precise alignment achieved by adjusting the distance between the lens and the target.

To monitor plasma properties and determine their parameters, spectral diagnostics were obtained from Ni metallic targets during ablation in 10 mL of deionized water. As shown in Fig. 1, an optical fibre positioned toward the discharge point collected the emission spectra of the plasma plume over the wavelength range 200–400 nm and directed them onto the spectrometer's entrance slit. The spectrometer (Thorlabs-CCS 100/M; $\Delta\lambda < 0.5$ nm) was utilized with an integration time of 2 ms and a delay time of 1μs to capture the plasma emission at its optimal intensity while minimizing continuum radiation. The generated nanoparticles in distilled water were dried at 70°C on glass slides for characterisation.

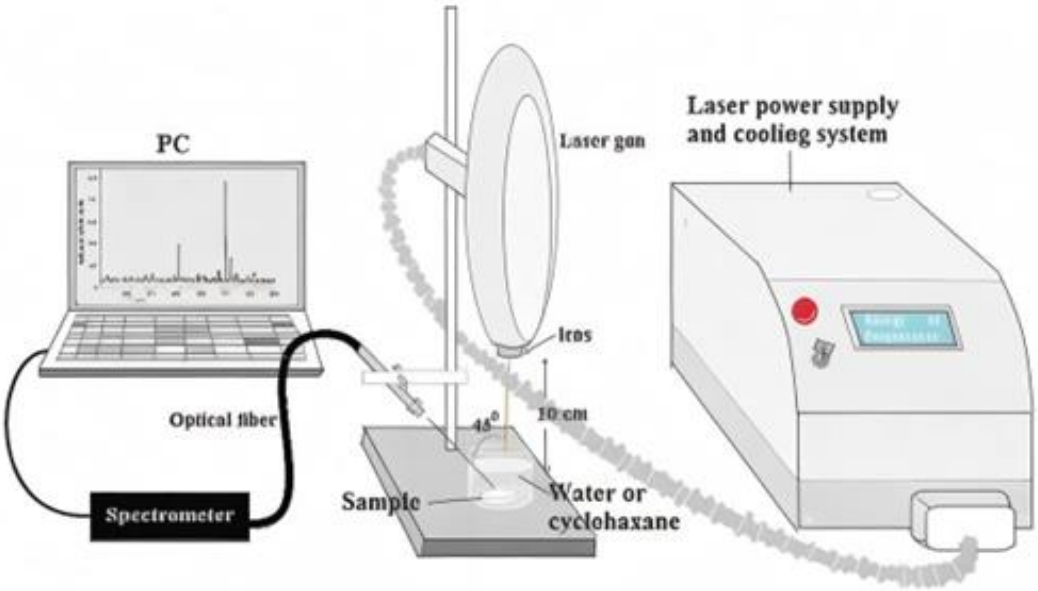

Figure 1- Schematic of the experimental setup for (LIBS) system.

X-ray diffraction (XRD) from SHIMATZU-6000 was used to examine the structural properties of the prepared nanoparticles with Cu-Kα emission and monochromatic wavelength $\lambda = 1.5405$ Å within the diffraction angle range 20-80°. The morphology of the prepared thin films was studied by a field emission scanning electron microscope (FE-SEM) (Inspect F 50-FEI Com.).

3. Results and Discussions

Fig. 2 illustrate the spectroscopic patterns of plasma induced by pulsed laser at different pulse energies from Ni target at different laser energies. The spectroscopic emission spectra obtained using LIBS with an Nd:YAG nanosecond pulsed laser at different pulse energies (600, 700, 800, and 900 mJ) are shown in Fig. 2. The spectra reveal significant variations in intensity, broadening, and species distribution. The ablation process is greatly affected by the higher electron temperature as it increases the kinetic energy of the ablated species, which improves atomic mobility during film formation [22]. The spectral lines identified in the emission spectra were matched with the standard emission in the NIST database [23], as indicated by the vertical reference

lines of neutral nickel (Ni I) emissions and singly ionized nickel (Ni II) emissions. A few emission lines corresponding to the ionized species with low intensity compared with those corresponding to Ni I indicate a low degree of ionization. The degree of ionization, defined as the ratio of ionized species (Ni II) to neutral species (Ni I), is influenced by the laser's increasing pulse energy. As the pulse energy increases from 600 – 900 mJ, the overall intensity of spectral lines increases, indicating stronger excitation and plasma formation by more energy deposited into the material, leading to higher plasma temperatures. This increase in temperature enhances collisional excitation processes, as stated by the Boltzmann distribution [24, 25].

The variation in intensities at different wavelengths can be attributed to the differences in excitation and transition probabilities of the emitting species. More substantial emission peaks in the ultraviolet range 200–400 nm correspond to highly excited states of nickel, which become more populated at higher laser energies. Spectral broadening is also observed, with more pronounced effects at higher pulse energies. The dominant emitted lines broadening mechanism is the Stark broadening due to high electron densities in the plasma and instrumental broadening.

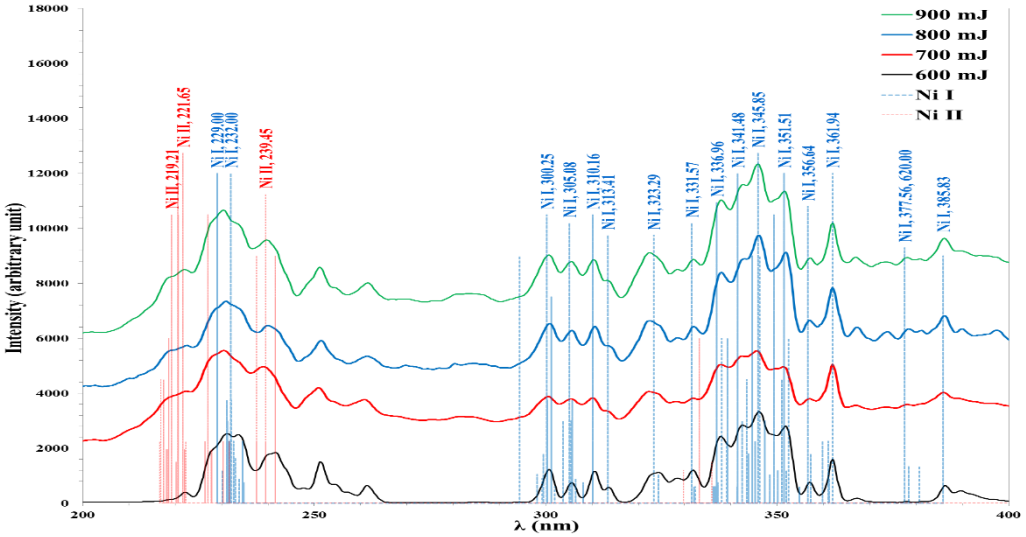

Figure 2: Emitted spectra for LIBS from Ni target using different pulsed laser energies.

The Boltzmann-Plot was used to determine the electron temperature using the emission lines of Ni I species at different laser pulse energies of 600, 700, 800, and 900 mJ, as shown in Fig. 3. The plasma excitation temperature increased with increasing laser energy, which reflects a more effective ionization and excitation of the plasma species [26]. As the laser energy rises, there is a more significant amount of energy absorbed by the material, which results in more collisions within the plasma. These collisions transfer energy more efficiently, increasing the population of excited states and raising the overall excitation temperature.

Higher laser energies also lead to a more intense laser-material interaction, creating a more robust and sustained plasma plume. This increased intensity enhances the ionization and excitation processes, raising the plasma density. A denser plasma implies that more atoms and ions are excited, increasing plasma excitation temperature.

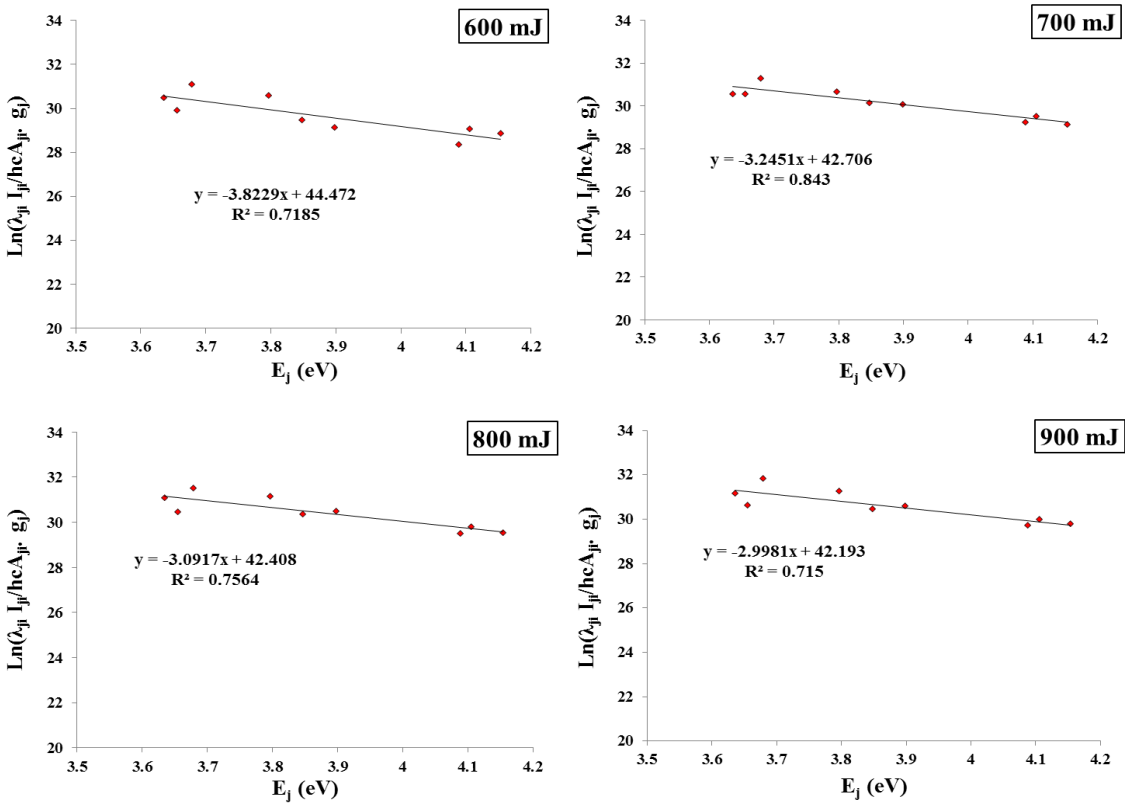

Figure 3: Boltzmann-plot using nine Ni I lines emission lines at different laser energies.

Fig. 4 displays the Lorentzian fit for the emitted Ni I line of λ=361.94 nm for the laser-induced plasma from the Ni target. The line broadening at different pulse energies (600, 700, 800, and 900 mJ) is beneficial in determining plasma density. The width of the spectral line appeared to be broader with the increase in laser energy. This broadening is dominated by Stark broadening and is associated with electron densities in the plasma. The fitted Lorentzian curves effectively describe the emission profile, capturing the peak intensities and widths at different laser energies.

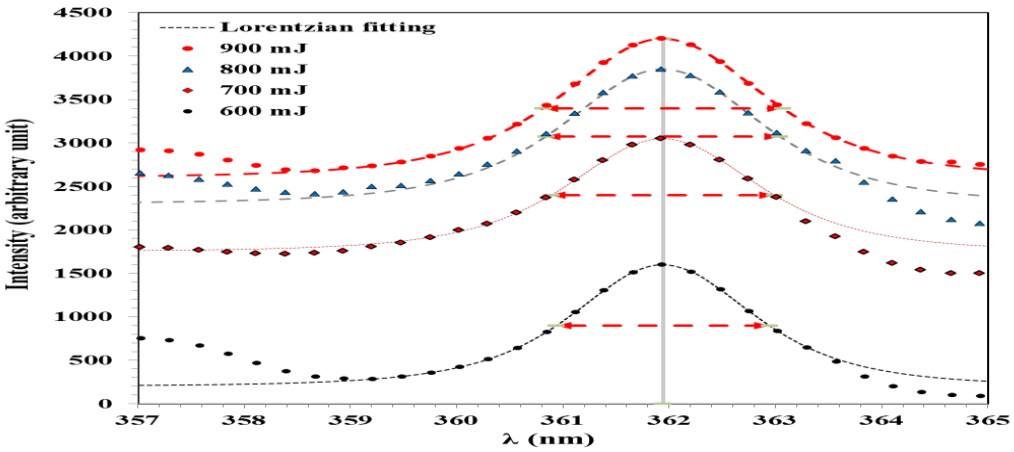

Figure 4: Lorentzian fit for emitted Ni I, 361.94 nm line for the laser-induced plasma at different pulse energies.

Table 1 lists the plasma parameters induced by the pulsed laser at different laser energies of (600, 700, 800, and 900 mJ). The electron temperature increases with laser energy, increasing from 0.262 eV at 600 mJ to 0.334 eV at 900 mJ. The increase in

electron temperature indicates more excellent ionization rates and enhanced excitation of plasma species. The electron density follows a similar trend, increasing from 5.00×10^{18} cm^{-3} to 5.63×10^{18} cm^{-3}. A higher electron density suggests increased ionized particles due to stronger laser-material interaction. The increased electron density contributes to enhanced plasma shielding effects, which may influence further laser absorption.

Similarly, plasma frequency increases with laser energy since it is directly related to electron density. The Debye length also exhibits an increasing trend with the increase in laser energy. A longer Debye length means a weaker electrostatic shielding effect around charged particles. This increase is consistent with rising electron temperature since the Debye length is proportional to the square root of the temperature-to-density ratio. The number of particles in a Debye sphere also increases. A higher number of particles in a Debye sphere indicates an ideal plasma behaviour,

Table 1: parameters of plasma induced by laser at different pulse energies

E (mJ)	T_e (eV)	$\Delta\lambda$ (nm)	$n_e \times 10^{18}$ (cm^{-3})	$f_p \times 10^{13}$ (Hz)	$\lambda_D \times 10^{-6}$(cm)	N_d
600	0.262	2.00	5.00	2.008	1.699	103
700	0.308	2.10	5.25	2.058	1.800	128
800	0.323	2.20	5.50	2.106	1.802	135
900	0.334	2.25	5.63	2.130	1.809	140

Fig. 5 illustrates the XRD patterns of the prepared NPs through the PLAL technique at different laser energies. The diffraction peaks are indexed to the crystallographic planes of Ni and NiO. These peaks match the face-centred cubic (FCC) structure of metallic Ni and the cubic structure of NiO. As the laser energy increases from 600 mJ to 900 mJ, the intensity of the diffraction peaks associated with metallic nickel (Ni) increases, suggesting improved crystallinity and larger crystallite sizes. The sharper peaks at higher energies indicate increasing the crystallite size. The presence of NiO alongside metallic Ni is evident in all the patterns, indicating partial oxidation during the PLAL process. The NiO peaks remain less intense than metallic Ni, demonstrating that Ni is the dominant phase.

The broad peak observed, especially at the low laser energy, indicates smaller crystallite sizes with possible lattice strain formation. As the laser energy increases, the peaks become less broadening and more intense due to the growth of larger nanoparticles. This change is due to enhanced ablation at higher laser energy, leading to significant evaporation of the target material and more development of nanoparticles. The variations observed in the XRD patterns correlate with the plasma emission characteristics obtained from LIBS. Increasing electron temperature and density enhances the crystallite size. Collisions with more electrons of higher energy may heat the created seed particles inside the plasma. The collected positive charge nanoparticles attract free electrons from the plasma, causing an increase in the collision frequency according to plasma density. These electrons act as heating sources during the nanoparticles' growth, delaying the cooling and enhancing crystallization [27].

The high temperature of plasma at high energy of pulsed laser causes an increase in oxidation, leading to the formation of nickel oxide. However, the short-lived nature of the plasma plume and rapid cooling in the liquid medium limit the extent of oxidation, resulting in the dominance of metallic Ni over NiO.

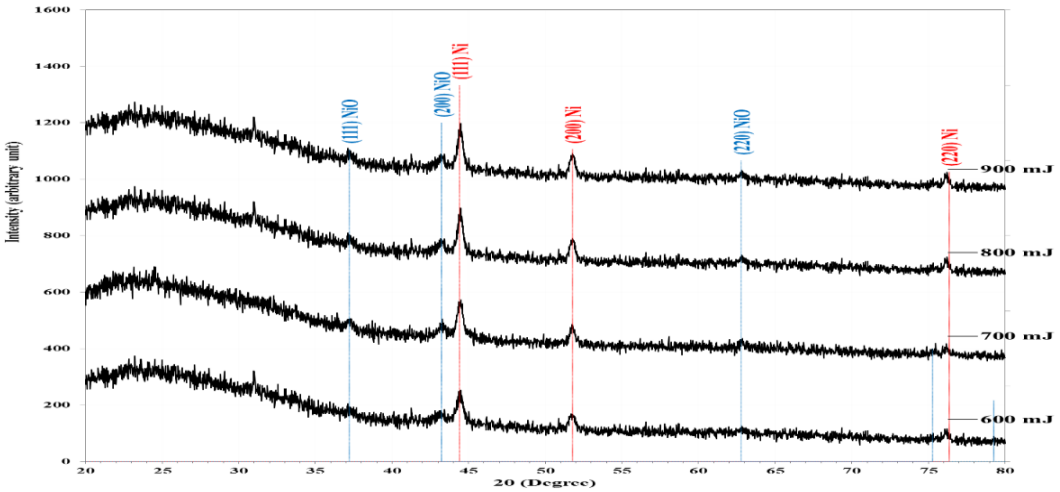

Figure 5: XRD of the prepared Ni:NiO NPs using different pulse laser energies.

The inter-planar spacing (d_{hkl}) was determined using the Bragg formula, Eq. (3) [28]:

$$n\lambda = 2d_{hkl}\sin\theta \quad (3)$$

where λ is the x-ray wavelength and θ is the diffraction angle.

The crystallite size was determined using Debye-Scherer formula, Eq. (4) [29]:

$$D = \frac{0.9\,\lambda}{\beta\,.\cos(\theta)} \quad (4)$$

where β is the breadth of the diffracted line at half maxima. While the lattice strain ($\boldsymbol{\varepsilon}$) was calculated using the relation, Eq. (5) [30]:

$$\varepsilon = \frac{\beta\,.\cot(\theta)}{4} \quad (5)$$

Table 2 lists the XRD parameters of Ni:NiO nanoparticles synthesized using different laser pulse energies. The crystallite size increases with higher laser energy, where the crystallite size grows from 17.3 nm at 600 mJ to 24.9 nm at 900 mJ, corresponding to the preferred orientation of Ni along the (111) direction. The interplanar spacing (d_{hkl}) shows slight variations with laser energy, reflecting strain and crystal defect changes. The data also show that higher laser energy promotes the formation of larger and more crystalline nanoparticles while reducing lattice strain. Fig. 6 displays the top-view FE-SEM images at two magnifications (30 kx and 120 kx) that were prepared at two different laser energies, 600 mJ and 900 mJ. At lower laser energy, the nanoparticles appear distributed with moderate agglomeration. The higher magnification images reveal particles with sizes ranging from approximately 28.29 to 48.73 nm. The distribution appears relatively uniform, although some larger aggregates are present. The lower laser energy likely results in less intense ablation, causing smaller particle sizes due to limited material ejection and a shorter plasma lifetime.

The images at 900 mJ energy show a greater density of nanoparticles with more agglomeration. At higher magnification, particle sizes range from 46.71 to 66.66 nm, indicating a broader size distribution with significant variation. The increased laser energy leads to a more intense ablation process, producing larger particles due to enhanced ablated substances. The elevated plasma temperature and extended plasma

lifetime at higher laser energy merge the adjacent nanoparticles, resulting in larger aggregates as cauliflower structures. The increase in particle size and agglomeration is consistent with the XRD patterns, where higher laser energy resulted in larger crystallite sizes and improved crystallinity. In addition, the increased ionization ratio (Ni II/Ni I) in the LIBS spectra causes more oxidizing processes.

Table 2: XRD parameters of Ni:NiO NPs at different pulse laser energies.

Laser Energy (mJ)	2θ°	FWHM	d_{hkl} (Å)	D (nm)	Phase	hkl	ε
	43.2260	0.4942	2.0913	17.3	Cub. NiO	(200)	0.0054
	44.4314	0.4964	2.0373	17.3	Cub. Ni	(111)	0.0053
600	51.7593	0.4811	1.7648	18.4	Cub. Ni	(200)	0.0043
	76.1601	0.5069	1.2489	19.9	Cub. Ni	(220)	0.0028
	43.2380	0.4203	2.0907	20.3	Cub. NiO	(200)	0.0046
700	44.4434	0.4768	2.0368	18.0	Cub. Ni	(111)	0.0051
	51.7713	0.4641	1.7644	19.0	Cub. Ni	(200)	0.0042
	76.1721	0.4690	1.2488	21.5	Cub. Ni	(220)	0.0026
	37.2279	0.4129	2.4133	20.3	Cub. NiO	(111)	0.0053
	43.2500	0.4093	2.0902	20.9	Cub. NiO	(200)	0.0045
800	44.4554	0.4217	2.0363	20.4	Cub. Ni	(111)	0.0045
	51.7833	0.4206	1.7640	21.0	Cub. Ni	(200)	0.0038
	62.8087	0.4512	1.4783	20.6	Cub. NiO	(220)	0.0032
	76.1841	0.4260	1.2486	23.7	Cub. Ni	(220)	0.0024
	37.2399	0.3825	2.4125	21.9	Cub. NiO	(111)	0.0050
	43.2620	0.3590	2.0896	23.8	Cub. NiO	(200)	0.0040
900	44.4674	0.3454	2.0358	24.9	Cub. Ni	(111)	0.0037
	51.7953	0.3819	1.7636	23.1	Cub. Ni	(200)	0.0034
	62.8207	0.3658	1.4780	25.5	Cub. NiO	(220)	0.0026
	76.1961	0.3940	1.2484	25.6	Cub. Ni	(220)	0.0022

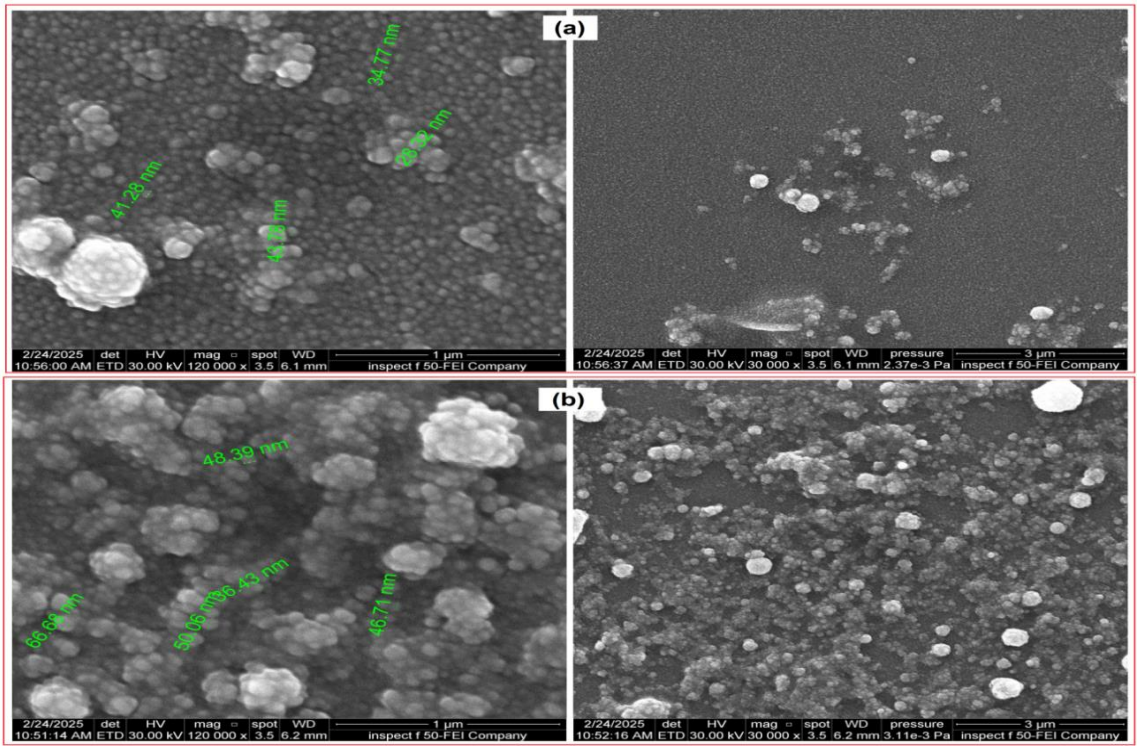

Figure 6: Top view FE-SEM images of the prepared Ni:NiO films at (a) 600 mJ and (b) 900 mJ pulse laser energies.

4. Conclusions

This study successfully establishes a quantitative correlation between laser pulse energy and the characteristics of both the generated plasma and the synthesized Ni/NiO nanoparticles. The LIBS spectra show a clear dependence on laser pulse energy, with higher energy leading to enhanced emission intensity, a higher ionization ratio, a higher excitation temperature, and a higher electron density. The ablation efficiency increased with higher laser energies. The increase in electron temperature and density led to more collisions, thereby improving the energy transfer to suspended particles. Additionally, plasma shielding effects may become more pronounced at higher energies, influencing subsequent laser-material interactions and enhancing crystallinity and larger-particle growth during nanoparticle formation. The joint analysis of OES and XRD demonstrates the precision of PLAL in controlling nanoparticle properties. Compared to chemical manufacturing methods, this methodology provides better control over purity and phase composition, making it suitable for catalytic applications where phase purity is critical. Laser energy significantly affects the morphology, average particle size, and aggregation behaviour of the synthesized nanoparticles. At lower energy, the particles are smaller and less aggregated; at higher energy, they are larger and more aggregated. The variation in crystalline structure and surface morphology directly influences physical and functional properties. Decreased crystallite size enhances surface morphology by particle aggregation and porosity, which is crucial for specific applications such as sensors and biomedical fields.

Conflict of Interest

The authors declare that they have no conflict of interest.

References

1. T . H. H. Murbat, N. KH. Abdalameer, A. Kh. Brrd, and F. Abdulameer, Bagh. Sci. J., **15**, 221 (2018). https://doi.org/10.21123/bsj.2018.15.2.0221.
2. I. HJ, K. A. Hubeatir, and K. A. Aadim. Sci. Rep. **13**, 5441 (2023). https://doi.org/10.1038/s41598-023-32330-z.
3. U. Baig, M. A. Ansari, M. A. Gondal, S. Akhtar, F. A. Khan, and W.S.Falath, Mater. Sci. Eng. C., **113**, 110992 (2020). https://doi.org/10.1016/j.msec.2020.110992.
4. A. A. Abed, A. S. Hameed, and M. O. Salman, J.Theor. Appl. Phys. **18** (2024). https://doi.org/10.57647/j.jtap.2024.si-AICIS23.20.
5. N. Baig, I. Kammakakam, and W. Falath, Mater. Adv. **2**, 1821 (2021). https://doi.org/10.1039/D0MA00807A.
6. P. Kathiravan, K. Thillaivelavan, G. Viruthagiri, and N. Shanmugam, J. Indian Chem. Soc. **101**, 101171 (2024). https://doi.org/10.1016/j.jics.2024.101171.
7. M. A. Dar, S. R. Majid, I. S. Imaduddin, M. Satgunam, M. R. Karim, and P.Arularasan, Int. J. Hydrogen Energy. **103**, 926 (2025). https://doi.org/10.1016/j.ijhydene.2025.01.270.
8. C. Montoro, J-Y .Kim, A. Mirzaei, J-H. Lee, S. Sayegh, E. Makhoul, I. Iatsunskyi, E. Coy, M. Bechelany, H.W. Kim, S. S. Kim, Compos. Part B: Eng. **283**, 111637 (2024). https://doi.org/10.1016/j.compositesb.2024.111637.
9. M. G. Mulla, and R. K. Pittala. Ceram. Int. **51**, 22255 (2025). https://doi.org/10.1016/j.ceramint.2025.02.387.
10. A. Ojeda, M. Döbeli, and T. Lippert. Adv. Mater. Interfaces. **5** , 1 (2018). https://doi.org/10.1002/admi.201701062.
11. G. M. Al-Senani, S. H. Alrefaee, A. N. Al-Ahmadi, M. M. ElFaham, A. R. Z. Almotairy, W. B. Elsharkawy, A. M. Mostafa. Radiat. Phys. Chemistry. **208**, 110872 (2023). https://doi.org/10.1016/j.radphyschem.2023.110872.
12. A. E. Fazio, B. Gökce, A. De Giacomo, M. Meneghetti, G. Compagnini, M. Tommasini, F. Waag, A. Lucotti , et al, Nanomaterials. **10**, 2317 (2020). https://doi.org/10.3390/nano10112317.
13. A. De Giacomo. Spectrochimica. Acta Part B. **58**, 71 (2003). https://doi.org/10.1016/S0584-8547(02)00234-3.
14. A. Ajith, M. N. S. Swapna, H. Cabrera, and I. S. Sankararaman. Photonics. **10**, 199 (2023). https://doi.org/10.3390/photonics10020199.

15. M. H. Mohsin, K. S .Khashan, and G. M. Sulaiman. Eur. Phys. J. B. **97**, 147 (2024). https://doi.org/10.1140/epjb/s10051-024-00783-4.
16. M. A. Gondal, T. A. Saleh, and Q. A. Drmosh, Appl. Surf. Sci. **258** , 6982 (2012) https://doi.org/10.1016/j.apsusc.2012.03.147.
17. A. Sergievskaya, A.O'Reilly, A.Chauvin, J. Veselý, A. Panepinto, J. De Winter, D. Cornil, J. Cornil, S. Konstantinidis. Colloids Surf. A, **615**, 126286 (2021). https://doi.org/10.1016/j.colsurfa.2021.126286.
18. A. Hanna, and E. Fisher. J. Vac. Sci. Technology. A. **38**, 20806 (2020). https://doi.org/10.1116/1.5141844.
19. M.Fikry, W.Tawfik, M.M.Omar. Optica Applicata, **51**, 248 (2021) https://doi.org/10.37190/oa210305
20. M.Fikry, W.Tawfik, and M.M.Omar, J. Mol. Struct., **1276**, 134796 (2022) https://doi.org/10.1016/j.molstruc.2022.134796.
21. M. El-Saeed, A.A. I. Khalil, M. Mubarak, M. Fikry, Sci. Rep., **15**, 19949 (2025). https://doi.org/10.1038/s41598-025-19949-0.
22. A. S. Maktoof and G. H. Mohammed, Iraqi J. Sci. **63**, 2502 (2022), https://doi.org/10.24996/ijs.2022.63.6.17.
23. *NIST Atomic Spectra Database*. (Online). Available: http://KineticsNistGov/IndexPhp, (2025).
24. K. A. Aadim, and R. H. Jassim. AIP Conf. Proc. **2372**, 080014 (2021). https://doi.org/10.1063/5.0067300.
25. H. Bolouki, P-H. Hsieh, C-H. Li, and M-C. Yang. Plasma. **2**, 283 (2019). https://doi.org/10.3390/plasma2030020.
26. S. Waheed, S.Bashir, G. Jose, R. Mathieson, E. K. Barimah, A. Hayat, M.R. Ayub, Optik. **324**, 172214 (2025). https://doi.org/10.1016/j.ijleo.2025.172214.
27. F. Taccogna, M. Dell'Aglio, M. Rutigliano, G. Valenza, and A. De Giacomo. Plasma Sources Sci. Technol. **26**, 045002 (2017). https://doi.org/10.1088/1361-6595/aa595b.
28. P. Tückmantel. *Scanning Probe Studies of Structural and Functional Properties of Ferroelectric Domains and Domain Walls*. (Springer International Publishing, 2021). https://doi.org/10.1007/978-3-030-72389-7
29. I. Dhanya, and B. Sasi, J. Coat. **2013**, 1 (2013). https://doi.org/10.1155/2013/981515.
30. A. A. Meji, D. Usha, and B. M. Ashwin. Mater. Res. Express. **11**, 085004 (2024). https://doi.org/10.1088/2053-1591/ad6d34.

ضبط خصائص البلازما لتخليق جسيمات النيكل النانوية المُتحكم بها من خلال الاستئصال بالليزر النبضي

أحمد موسى علوان[1] و أحمد عبدالرزاق نعمة[2]
[1,2] قسم الفيزياء، كلية العلوم، جامعة بغداد، بغداد، العراق

الخلاصة
تُجري هذه الدراسة بحثًا منهجيًا حول العلاقة بين معايير البلازما والخصائص البنيوية لجزيئات النيكل النانوية المُصنّعة بتقنية الاستئصال الليزري النبضي في السائل (PLAL) عند طاقات ليزر مُتفاوتة تتراوح بين 600 و900 ملي جول. وكشف التحليل الطيفي للانبعاث الضوئي (OES) أن زيادة طاقة الليزر تُعزز تأين البلازما، حيث ترتفع درجة حرارة الإلكترون (T_e) من 0.262 إلى 0.334 إلكترون فولت، وتزداد كثافة الإلكترون (n_e) من 5.00×10^{18} إلى 5.63×10^{18} سم$^{-3}$ نتيجةً لزيادة الإثارة التصادمية. وقد أثرت ظروف البلازما بشكل مباشر على تغيرات حجم وشكل البلورات، مُبينةً أن ارتفاع درجات الحرارة والكثافة في البلازما يُؤدي إلى جزيئات نانوية أكبر حجمًا وأكثر انتظامًا. وأظهر تحليل حيود الأشعة السينية (XRD) تكوّن كلٍ من النيكل المعدني (Ni) وأكسيد النيكل (NiO)، كما ازداد حجم البلورات من 17.3 إلى 25.6 نانومتر. أظهر المجهر الإلكتروني الماسح للانبعاث الميداني (FE-SEM) أنه مع زيادة طاقة البلازما، ازداد حجم الجسيمات النانوية من 28.29 إلى 48.73 نانومتر عند 600 ملي جول ومن 46.71 إلى 66.

الكلمات المفتاحية: تقنية الاستئصال الليزري النبضي في السائل، التحليل الطيفي للانبعاث الضوئي، خصائص البلازما، جسيمات النيكل النانوية، الخصائص التركيبية.